

A Fourier-Space Approach to Physics-Informed Magnetization Reconstruction from Nitrogen-Vacancy Measurements

Alexander Setescak,^{1, a)} Florian Bruckner,¹ Dieter Suess,¹ Young-Gwan Choi,^{2,3} Hayden Binger,² Lotte Boer,² Claire Donnelly,² Uri Vool,² and Claas Abert¹

¹⁾ *University of Vienna, Vienna, Austria*

²⁾ *Max Planck Institute for the Chemical Physics of Solids, Dresden, Germany*

³⁾ *University of Ulsan, Ulsan, Republic of Korea*

(Dated: 20 February 2026)

Reconstructing complex magnetization textures from nitrogen-vacancy (NV) magnetometry stray-field measurements presents a challenging inverse problem. In this work, we introduce a physics-informed method that addresses this by incorporating the full micromagnetic energy directly into the variational formulation. Built on a PyTorch backend, our forward model integrates an auto-differentiable finite-differences micromagnetic framework with FFT-based stray-field calculations and Fourier-space upward continuation. This enables efficient gradient-based optimization via the adjoint method and allows the sensor-sample distance to be treated as an optimization parameter. By doing so, we eliminate the experimental uncertainty arising from unknown NV implantation depths and surface oxidation layers. Validation on synthetic data demonstrates high-fidelity reconstruction of spin textures and precise sensor height estimation. Furthermore, when applied to NV measurements of the van der Waals ferromagnet $\text{Fe}_{3-x}\text{GaTe}_2$, the method reconstructs the previously unknown NV-sample distance and physically plausible magnetization textures, which accurately reproduce the experimental observations.

I. INTRODUCTION

Many recent developments in stray-field measurement techniques have enabled the exploration of nanoscale magnetic textures. Among these, nitrogen-vacancy (NV) magnetometry (Fig. 1a) has emerged as a powerful tool: It uses nitrogen-vacancy centers in diamond as atomic-scale quantum sensors. The fluorescence (light emission) from these sensors changes based on their spin state, allowing for the highly sensitive and quantitative measurement of magnetic fields^{1,2}. However, inferring the underlying magnetization from measured stray fields constitutes an ill-posed inverse problem^{1,3,4}: infinitely many magnetization configurations can produce the same stray field (Fig. 1b). This ambiguity is a hallmark of magnetic inverse problems, also posing significant challenges in the reconstruction of current densities from magnetic field maps⁵. Approaches to solving this inverse problem have evolved across different methodologies. Early work by Hug et al.⁶ established quantitative Magnetic Force Microscopy (qMFM) by determining an instrument calibration function to analytically deconvolve the stray field data. This approach effectively reconstructs the magnetic surface charge equivalent, providing a quantitative map of the field sources at the sample surface⁷. In contrast, Bruckner et al.⁴ formulated the reconstruction as a variational optimization task. Their approach utilizes the adjoint method and Tikhonov regularization to reconstruct the 3D magnetization by minimizing the field residual via gradient-based optimization. Yao et al.⁸ additionally incorporates topological charge constraints to successfully reconstruct different magnetic quasiparticles. Simultaneously, the integration of deep learning has further advanced the field. Physically-informed neural networks have

^{a)}Electronic mail: alexander.setescak@univie.ac.at

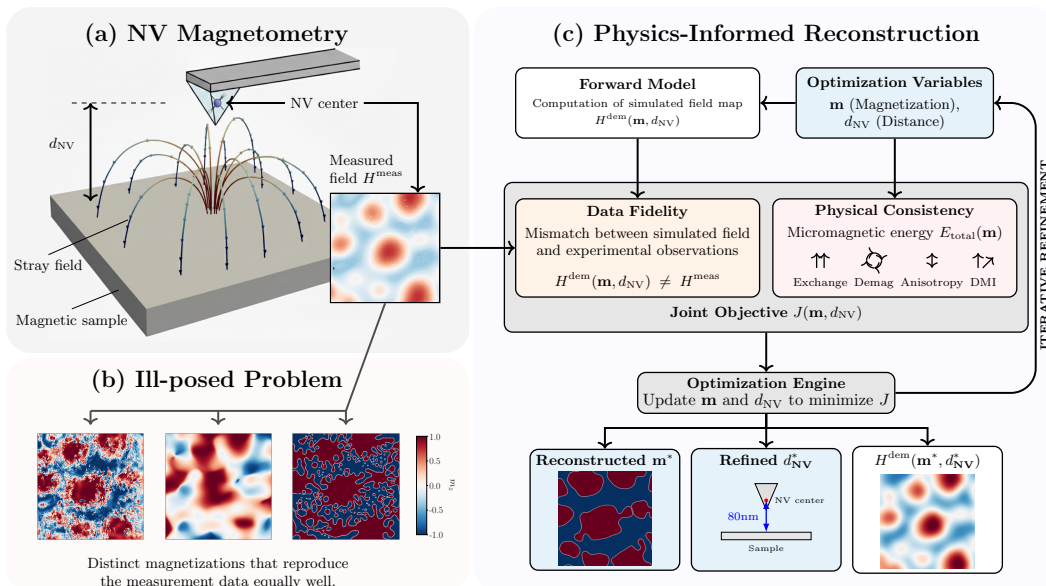


FIG. 1: **Physics-informed reconstruction of magnetization textures from NV magnetometry.** The schematic illustrates the workflow for overcoming the ill-posed nature of stray-field imaging. **(a)** NV magnetometry measures the stray field projection H^{meas} at a unknown distance d_{NV} from the sample. **(b)** Multiple distinct magnetization configurations can produce a nearly identical stray field, making direct inversion unreliable. **(c)** Our physics-informed framework solves this by coupling a differentiable forward model with a joint objective function. This objective balances data fidelity with micromagnetic energy. Through iterative gradient-based optimization, the framework simultaneously reconstructs the magnetization \mathbf{m} and refines the sensor distance d_{NV} . This yields the final parameters \mathbf{m}^* and d_{NV}^* as an energetically favorable configuration that remains consistent with the experimental observations.

proven effective in reconstructing magnetization configurations^{9,10}. The network’s architecture naturally enforces smoothness, while the field based forward loss enables the recovery of the magnetization. However, when applied to fully three-dimensional spin textures, successful reconstruction remains challenging and requires an initial magnetization guess⁹. Recently, we introduced a hybrid strategy¹¹ that utilizes a U-Net to generate an initial guess, followed by micromagnetic relaxation. While this approach is very effective at recovering intrinsic material parameters, it relies on a multistep process that fundamentally separates the data-driven estimation from the final physics-based refinement. Here, we propose a powerful alternative to existing reconstruction strategies: a self-consistent physics-informed reconstruction framework that embeds micromagnetic physics directly into the optimization (Fig. 1c). Compared to other variational methods that rely on mathematical regularization as a proxy for physics, e.g. using Tikhonov regularization as a qualitative exchange interaction, we replace these heuristic regularizers with quantitative micromagnetic energy terms. This leaves us with a single regularization weight that balances the magnetic stray field residual against the system’s total energy, and can be optimally selected with the so-called L-Curve method^{12,13}. This yields a transparent, end-to-end optimization process that requires no training data and provides quantitative reconstruction of nanoscale magnetic texture along with critical experimental parameters, such as the sample-sensor distance.

II. METHODS

A. Forward Model

Given the magnetization of the sample, our forward model essentially simulates what an NV magnetometer would detect at a certain distance from the sample. It provides us with a differentiable map from a given magnetization configuration \mathbf{m} and the distance d_{NV} to the expected signal. The required micromagnetic calculations are performed using the open-source, finite-difference Python library `magnum.np`¹⁴. This GPU-accelerated PyTorch-based code efficiently evaluates the stray field through FFT convolution with the demagnetization tensor kernel, resulting in a favorable computational complexity of $\mathcal{O}(N \log N)$.

All simulations presented in this study focus on an $800 \text{ nm} \times 800 \text{ nm}$ area of a $\text{Fe}_{3-x}\text{GaTe}_2$ flake of thickness 100 nm . The system is discretized with a cell size of $\Delta_x = \Delta_y = 1 \text{ nm}$ and $\Delta_z = 100 \text{ nm}$. The geometry consists of two layers: the bottom layer represents the magnetic material, while the top layer is set to vacuum to calculate stray fields above the sample surface. For a detailed description of the simulation setup see Appendix B.

The solver `magnum.np` computes the stray field averaged over the simulation cell volume ($1 \text{ nm} \times 1 \text{ nm} \times 100 \text{ nm}$). While lateral spatial averaging is negligible, the vertical averaging over the vacuum layer thickness Δ_z introduces significant deviations that require explicit correction to enable comparison with measurements performed at a specific sensor height d_{NV} . Fortunately, in the non-magnetic region $z > z_0$ above the sample surface z_0 , the magnetic field satisfies Laplace's equation, permitting the derivation of an exact transfer function in 2D Fourier space (see Appendix C). Starting with the averaged field $\langle \mathbf{H}^{\text{dem}} \rangle_{[z_0, z_0 + \Delta_z]}$ in the vacuum layer above the sample, this function recovers the magnetic field at the sample surface and extrapolates it to the NV sensor height d_{NV} :

$$\tilde{\mathbf{H}}^{\text{dem}}(d_{\text{NV}}) = \underbrace{\langle \tilde{\mathbf{H}}^{\text{dem}} \rangle_{[z_0, z_0 + \Delta_z]}}_{\text{De-averaging}} \cdot \underbrace{\left(\frac{k\Delta_z}{1 - e^{-k\Delta_z}} \right)}_{\text{Upward continuation}} \cdot \underbrace{e^{-k(d_{\text{NV}} - z_0)}}_{\text{Upward continuation}}, \quad (1)$$

where $k = \sqrt{k_x^2 + k_y^2}$ is the magnitude of the wavevector and $\tilde{\mathbf{H}}^{\text{dem}}$ denotes the stray field in the 2D Fourier domain.

After upward continuation, the resulting vector field $\tilde{\mathbf{H}}^{\text{dem}}(d_{\text{NV}})$ is transformed back to real space via inverse FFT and projected onto the nitrogen-vacancy (NV) center quantization axis $\mathbf{n}_{\text{NV}} \approx (\sin 55^\circ, 0, \cos 55^\circ)$, which is determined by the diamond lattice structure¹⁵:

$$H^{\text{dem}} = \mathbf{H}^{\text{dem}} \cdot \mathbf{n}_{\text{NV}}. \quad (2)$$

This process yields a final scalar field map that can be directly compared to experimental measurement field maps.

Notably, our approach decouples the simulation's vertical discretization (Δ_z) from the measurement geometry. This allows for the modeling of thick magnetic samples using coarse discretization while accurately calculating the stray field at arbitrary sensor-sample distances. Furthermore, because the entire forward pipeline is implemented in PyTorch in a fully differentiable manner, it enables gradient-based optimization for not only the magnetization field \mathbf{m} but also for auxiliary parameters such as the NV sensor distance d_{NV} .

B. Physics-Informed Loss Functional

To solve the inverse problem of recovering the magnetization field \mathbf{m} from the measured field H^{meas} , we formulate an optimization problem by minimizing the loss functional $J(\mathbf{m}, d_{\text{NV}})$:

$$J(\mathbf{m}, d_{\text{NV}}) = \mathcal{L}_{\text{data}}(\mathbf{m}, d_{\text{NV}}) + \hat{\lambda} E_{\text{total}}(\mathbf{m}). \quad (3)$$

The first term $\mathcal{L}_{\text{data}}$ enforces data fidelity by quantifying the mismatch between the reconstructed and measured fields. It is explicitly defined as the mean absolute error (MAE) over the $N = N_x \times N_y$ measurement grid points:

$$\mathcal{L}_{\text{data}}(\mathbf{m}, d_{\text{NV}}) = \frac{1}{N} \sum_{i=1}^N |H_i^{\text{dem}}(\mathbf{m}, d_{\text{NV}}) - H_i^{\text{meas}}|, \quad (4)$$

where the index i runs over all pixels of the measurement. The second term, E_{total} , serves as a physics-informed regularization by penalizing high-energy micromagnetic states.

Following the micromagnetic framework of Abert et al.¹⁶, we define the total energy over the magnetic material domain Ω as the sum of four contributions: the exchange energy (E^{ex}), the demagnetization energy (E^{dem}), the uniaxial anisotropy energy (E^{aniu}), and the interfacial Dzyaloshinskii–Moriya interaction energy (E^{dmii}). These contributions are given by

$$\begin{aligned} E_{\text{total}}(\mathbf{m}) = & \underbrace{\int_{\Omega} A |\nabla \mathbf{m}|^2 dV}_{E^{\text{ex}}} \\ & - \underbrace{\frac{\mu_0 M_s}{2} \int_{\Omega} \mathbf{m} \cdot \mathbf{H}^{\text{dem}} dV}_{E^{\text{dem}}} \\ & - \underbrace{\int_{\Omega} K_u (\mathbf{m} \cdot \mathbf{e}_u)^2 dV}_{E^{\text{aniu}}} \\ & + \underbrace{\int_{\Omega} D_i [\mathbf{m} \cdot \nabla (\mathbf{e}_d \cdot \mathbf{m}) - (\nabla \cdot \mathbf{m})(\mathbf{e}_d \cdot \mathbf{m})] dV}_{E^{\text{dmii}}}. \end{aligned} \quad (5)$$

Here, A denotes the exchange stiffness constant, μ_0 the vacuum permeability, M_s the saturation magnetization, K_u the uniaxial anisotropy constant, and D_i the interfacial DMI constant. The unit vectors \mathbf{e}_u and \mathbf{e}_d define the uniaxial anisotropy axis and the interface normal direction, respectively. In the present study, both directions coincide with the out-of-plane direction, i.e., $\mathbf{e}_u = \mathbf{e}_d = \mathbf{e}_z$. The material parameters used throughout this work are $D_i \approx -0.51 \text{ mJ m}^{-2}$, $M_s \approx 53 \text{ kA m}^{-1}$, $K_u \approx 0.302 \text{ MJ m}^{-3}$, and $A \approx 0.70 \text{ pJ m}^{-117}$ (refer to Appendix B 1 for the full parameter derivation). Notably, E_{total} is evaluated on the same simulation setup used for the calculation of the forward model H^{dem} described in Section II A. The regularization parameter is defined as $\hat{\lambda} = \lambda \cdot \lambda_{\text{unit}}$, where $\lambda_{\text{unit}} = 1 \text{ A J}^{-1} \text{ m}^{-1}$ ensures dimensional consistency and $\lambda > 0$ is a dimensionless scaling factor. This factor controls the trade-off between data fidelity and physical stability. We determine the optimal λ using the L-Curve method¹², plotting the data mismatch $\mathcal{L}_{\text{data}}$ against the regularization energy E_{total} for varying λ . The "corner" of the resulting L-Curve identifies the optimal balance, providing a data-driven selection criterion.

C. Gradient-Based Minimization

The loss $J(\mathbf{m}, d_{\text{NV}})$ from Eq. (3) is minimized using PyTorch’s automatic differentiation¹⁸. Both the magnetization field \mathbf{m} and the sensor–sample distance d_{NV} are optimized jointly. We initialize $\mathbf{m}_0 = \mathbf{0}$, ensuring that the solution is guided exclusively by stray field data gradients. The optimization follows an iterative procedure:

1. **Forward Pass:** Compute the demagnetizing field $H^{\text{dem}}(\mathbf{m}, d_{\text{NV}})$ and total energy $E_{\text{total}}(\mathbf{m})$.
2. **Loss Evaluation:** Using these quantities evaluate the loss $J(\mathbf{m}, d_{\text{NV}})$.
3. **Backward Pass:** PyTorch autodiff computes the gradients $\nabla_{\mathbf{m}}J$ and $\nabla_{d_{\text{NV}}}J$, capturing sensitivities with respect to both magnetization and the sensor distance.
4. **Update:** Based on past gradients, an update step is taken for \mathbf{m} and d_{NV} to reduce J .

The procedure iterates until a stopping condition (e.g., convergence or maximum number of epochs) is met, yielding the optimized quantities \mathbf{m}^* and d_{NV}^* . The final state is required to satisfy the micromagnetic normalization constraint $|\mathbf{m}| = 1$. Instead of introducing another penalty term to the loss functional, we enforce this constraint by optimizing \mathbf{m} directly on the unit sphere manifold using **Riemannian Adam** optimizer (as implemented in the `geopt` library¹⁹). In contrast to standard **Adam**²⁰, which operates in Euclidean space, this approach adapts the algorithm to manifolds by (1) projecting the gradient onto the manifold surface, (2) performing the update step within this constrained space, and (3) retracting the result back onto the manifold. A similar result can be achieved by reparameterizing the magnetization in spherical coordinates, as in Suess et al.¹¹. However, unlike the Cartesian formulation, spherical coordinates require the specification of initial angles, introducing an inherent initialization bias.

Documentation on implementing such inverse problems within `magnum.np`, including a simplified demonstration of the magnetization reconstruction from magnetic field data, is available in the official library documentation²¹.

III. RESULTS

A. Validation with Synthetic Data

We first validate the reconstruction framework using synthetic data. The simulated measurement signal H^{meas} was generated from a ground-truth magnetization state \mathbf{m}_{ref} , assuming a sensor height of $d_{\text{NV,ref}} = 80$ nm (see Fig. 2). To simulate measurement noise, we perturbed this signal with additive Gaussian noise scaled to a fraction $\alpha = 0.03$ of its root-mean-square amplitude. This noisy synthetic signal was then used as input for the reconstruction.

Starting from an initial height estimate of $d_{\text{NV},0} = 70$ nm, we perform a joint optimization of both the magnetization field \mathbf{m} and the sensor height d_{NV} .

We used an L-Curve analysis (Fig. 3(a)) to determine the optimal regularization parameter, $\lambda_{\text{opt}} = 2.2 \times 10^{17}$.

Using λ_{opt} , the final reconstructed magnetization state \mathbf{m}^* (Fig. 4) shows excellent agreement with the reference state \mathbf{m}_{ref} , with only some small lateral shifts in the position of the domain walls. As seen in the m_x and m_y components, the chirality matches \mathbf{m}_{ref} , demonstrating that the internal structure of the Néel walls is accurately recovered. In contrast, a purely data-driven reconstruction ($\lambda = 0$) results in an unphysical state (Fig. 4).

Notably, as shown in Fig. 3(b), the reconstructed sensor height d_{NV}^* converges close to the correct ground-truth value $d_{\text{NV,ref}} = 80$ nm for a broad range of λ values, but the discrepancy increases especially for the over-regularized case for values closer to λ_{high} .

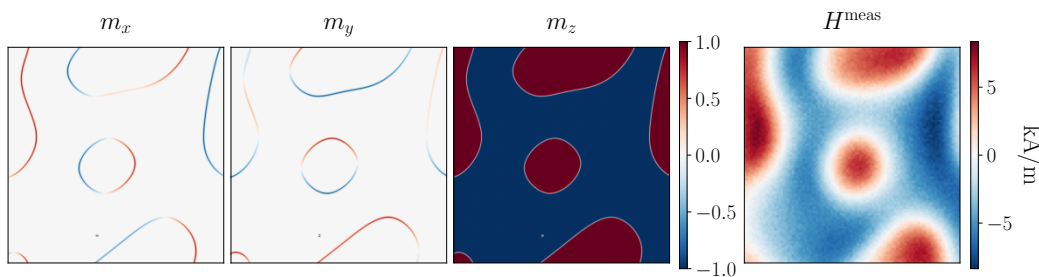


FIG. 2: **Synthetic data generation.** Individual components (m_x, m_y, m_z) of reference magnetization \mathbf{m}_{ref} and the corresponding stray field map H^{meas} that an NV sensor would sense at a sensor distance of $d_{\text{NV,ref}} = 80$ nm, including additive Gaussian noise scaled to 3% of the RMS signal amplitude.

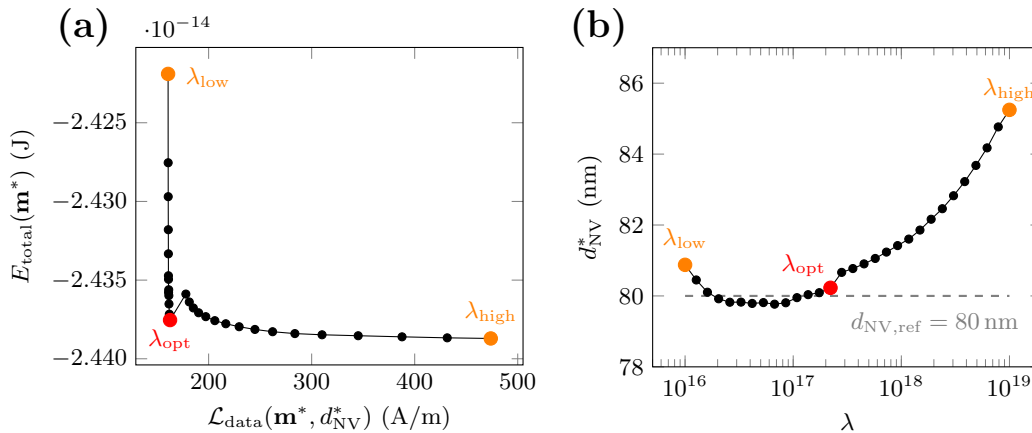


FIG. 3: **L-curve analysis for synthetic measurement data.** (a) The characteristic L-Curve illustrates the trade-off between field mismatch and total energy, identifying the optimal regularization parameter $\lambda_{\text{opt}} = 2.2 \times 10^{17}$. (b) Converged sensor height d_{NV}^* as a function of the regularization parameter λ .

B. Application to Experimental Data

Following synthetic validation, the workflow was applied to an experimental NV magnetometry measurement shown in Fig. 5. The measurements were performed at room temperature on $\text{Fe}_{3-x}\text{GaTe}_2$ flakes, synthesized and characterized as described in Zhang et al¹⁷. All measurements were conducted under a uniform external bias field of $H^{\text{bias}} \approx 3.2 \text{ kA m}^{-1}$. We observed characteristic measurement artifacts in regions where the opposing stray field locally exceeded this bias field, a consequence of the Optically Detected Magnetic Resonance (ODMR) sign ambiguity. This phenomenon is discussed in greater detail in Section A of the Supplementary.

The reconstruction jointly optimizes \mathbf{m} and d_{NV} using the measured stray field map H^{meas} as input. Figure 6 shows (a) the L-Curve analysis and (b) the corresponding variation of the converged sensor height d_{NV}^* . The analysis identifies an optimal regularization strength of $\lambda_{\text{opt}} = 2.8 \times 10^{17}$, which yields an optimized sensor height of $d_{\text{NV}}^* \approx 80$ nm. We observe that d_{NV}^* remains relatively stable between λ_{low} and λ_{opt} , trending toward 75 nm at the lower bound. In contrast, for values larger than λ_{opt} , the optimized height significantly increases, reaching up to 131 nm for λ_{high} .

To assess the impact of λ , three representative reconstructions are compared in Fig. 7. For a low regularization value ($\lambda_{\text{low}} = 1.0 \times 10^{16}$), the solution exhibits complex, fine-scale

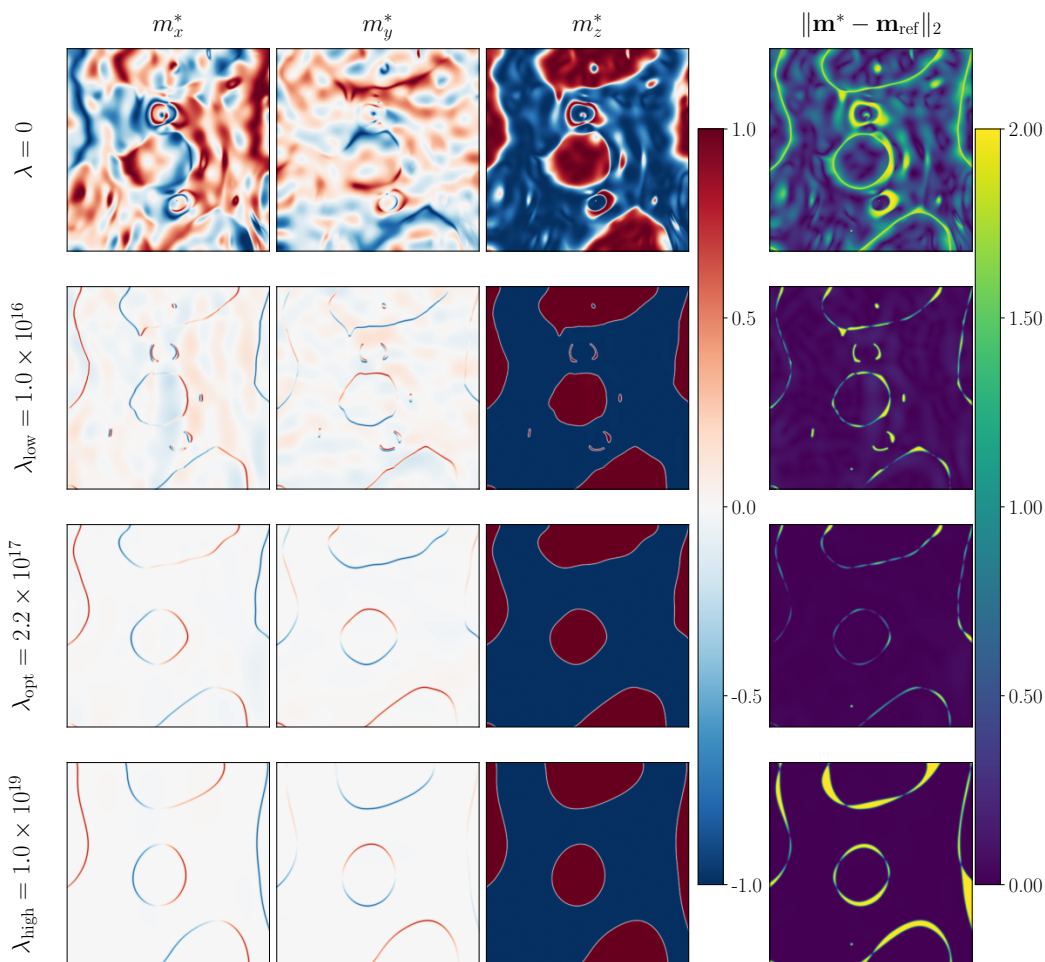


FIG. 4: **Impact of regularization strength on magnetization reconstruction accuracy.** In the unconstrained case, the reconstruction is highly diffuse and exhibits a large deviation from the ground truth. The optimal parameter, $\lambda_{\text{opt}} = 2.2 \times 10^{17}$, providing the best balance between data fidelity and physical consistency also corresponds to the reconstruction with the minimum L2 error norm, $\|\mathbf{m}^* - \mathbf{m}_{\text{ref}}\|_2$.

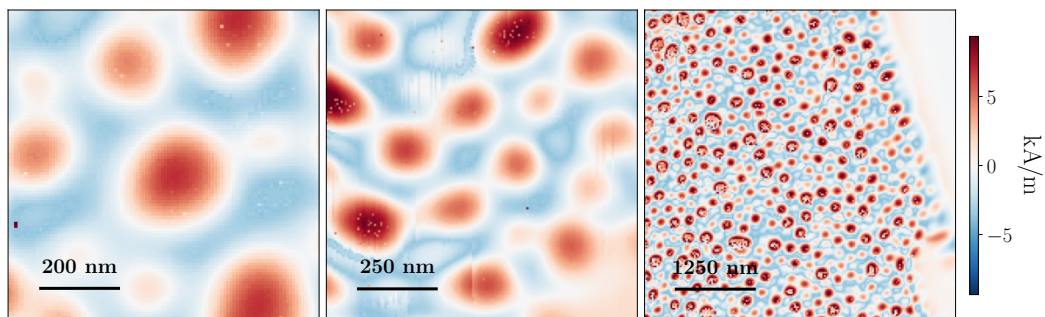


FIG. 5: **Experimental NV magnetometry measurements of a 100 nm thick $\text{Fe}_{3-x}\text{GaTe}_2$ thin film.** The measurements are displayed from left to right with scan areas of: (1) $800 \times 800 \text{ nm}^2$ (100×100 pixels); (2) $1000 \times 1000 \text{ nm}^2$ (150×150 pixels); and (3) $5000 \times 5000 \text{ nm}^2$ (200×200 pixels). The exact NV sensor-sample distances are unknown. The first field map H^{meas} (left) was used for the magnetization reconstruction in this work.

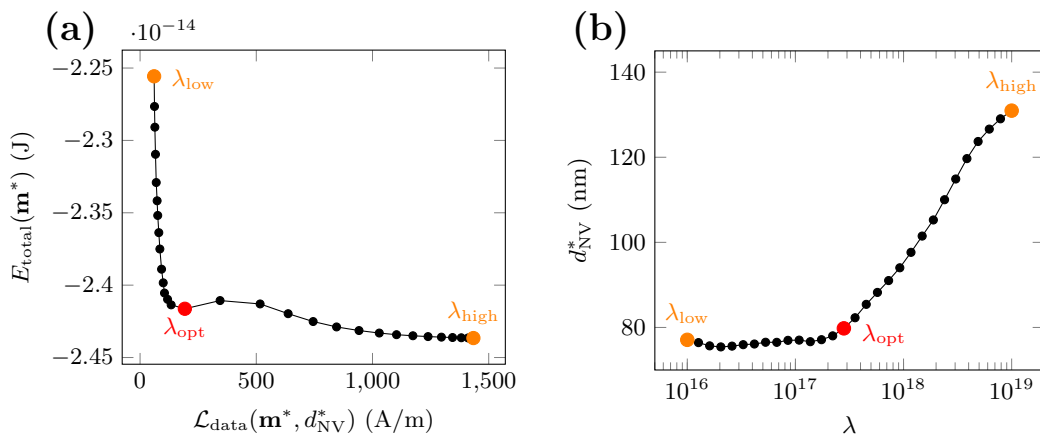


FIG. 6: **L-curve analysis for experimental measurement data.** (a) The characteristic L-Curve illustrates the trade-off between field mismatch and total energy, identifying the optimal regularization parameter $\lambda_{\text{opt}} = 2.8 \times 10^{17}$. (b) Converged sensor height d_{NV}^* as a function of the regularization parameter λ .

variations in m_z . Conversely, at a high value ($\lambda_{\text{high}} = 1.0 \times 10^{19}$), the magnetization textures appear very smooth, qualitatively resembling states expected from standard micromagnetic simulations. However, this solution fails to capture the specific features of the measured field. At λ_{opt} , the reconstructed magnetization \mathbf{m}^* tries to balance these extremes, minimizing the micromagnetic energy, while still reproducing the measured field map fairly well.

IV. DISCUSSION

The presented results demonstrate the capabilities of the joint optimization framework for both synthetic and experimental scenarios. The synthetic validation highlights the necessity of physics-informed regularization: while the unconstrained data-driven approach ($\lambda = 0$) yields an unphysical state, the method successfully captures complex magnetic textures, such as Néel Skyrmions, when λ_{opt} is used. The stability of the reconstruction across a range of regularization parameters indicates that the method is robust against minor parameter tuning errors. However, the highly non-convex nature of the loss landscape means that the optimization can be susceptible to local minima. This is particularly relevant when the sensor is positioned far from the sample or when the resolution is low; in these cases, the ambiguity of the inverse problem increases, resulting in many potential magnetization configurations producing similar signals.

A key experimental finding is the convergence of the sensor height to $d_{\text{NV}}^* \approx 75-80$ nm. Consistent with experimental estimates, this value remains stable for all $\lambda \leq \lambda_{\text{opt}}$, mirroring the robust plateau behavior observed in reconstructions from synthetic data. Physically, this distance corresponds to the total effective separation between the magnetic material and the NV center sensor, comprising the sample's oxidation layer, the physical gap, and the NV center's implantation depth²². Since all of these are often unknown in experiments, our ability to determine the total effective d_{NV}^* directly from measurement data solves a significant challenge and eliminates the need for separate calibration procedures. Conversely, for regularization strengths above λ_{opt} , the optimizer is forced to favor a strictly physical solution, which may not perfectly align with the experimental data. To compensate, the system increases d_{NV}^* to artificially dampen the calculated stray field. While this actually minimizes the residual field error in this case, it results in a field that is clearly weaker than the actual measurement, as observed in Fig. 7 for the over-regularized case λ_{high} .

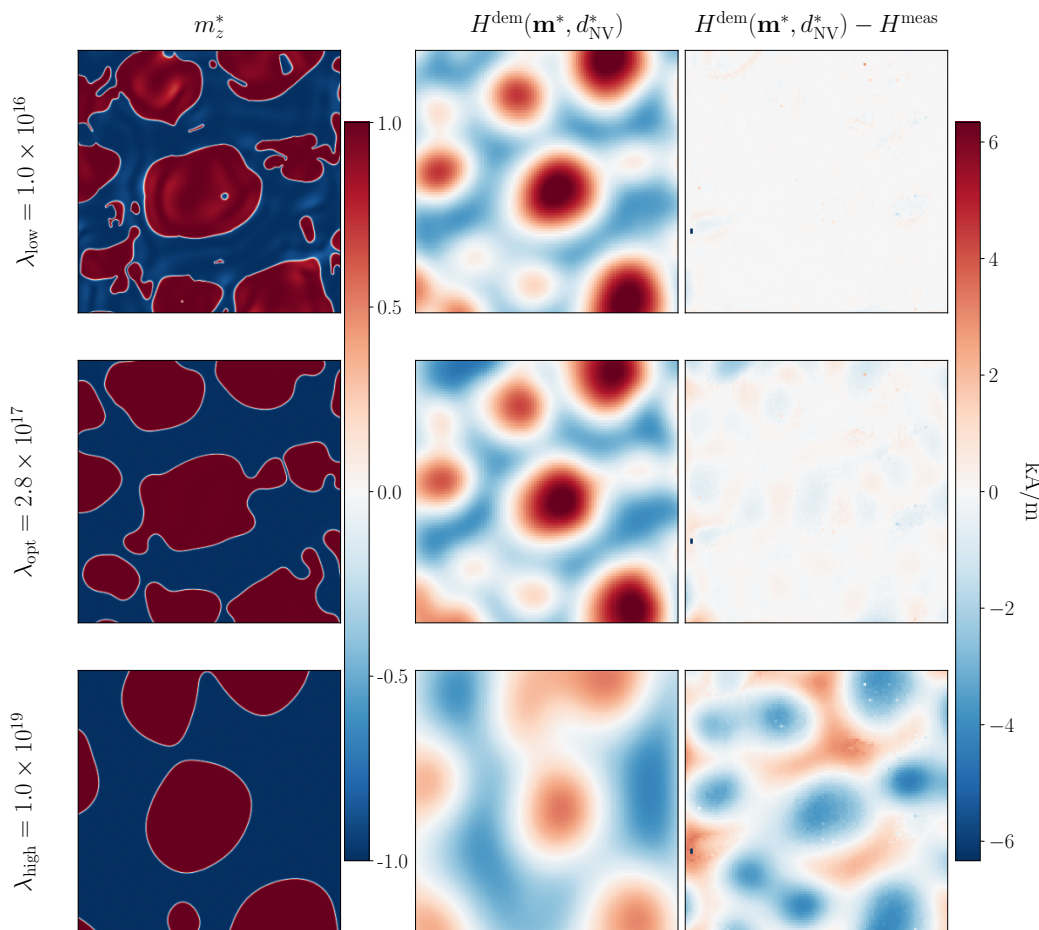


FIG. 7: **Influence of regularization strength λ on reconstructed magnetization and field maps.** Comparison between reconstructed magnetizations \mathbf{m}^* and their corresponding demagnetizing fields $H^{\text{dem}}(\mathbf{m}^*, d_{\text{NV}}^*)$ across varying λ . While higher regularization yields a less diffuse \mathbf{m}^* , it results in a poorer fit to the experimental field. At high λ values, the field strength is significantly underestimated, indicating a decoupling from the experimental data in favor of the regularization term.

Despite these successful demonstrations, the current model relies on the assumption of a homogeneous film with constant material properties and uniform thickness. These likely explain the behavior observed in the under-regularized regime. In local regions where the actual sample exhibits defects such as lower saturation magnetization or reduced thickness the optimizer can't adjust the physical constants. Instead, it compensates by fragmenting the magnetization into artificial micro-domains. These localized structures effectively lower the net averaged magnetization to match the weaker stray-field intensity found in some regions. Therefore, even with optimally chosen regularization (λ_{opt}), such micro-domains are likely artifacts rather than genuine physical features. Although the framework could theoretically resolve z -dependent variations, doing so would significantly increase the degrees of freedom for minimal practical benefit, given that the stray field signal from deeper layers is suppressed by exponential decay.

Furthermore, an important consideration regarding the reconstructed magnetization states is their stability under Landau-Lifshitz-Gilbert (LLG) relaxation^{14,23,24}. When optimized configurations \mathbf{m}^* are used as initial states for subsequent micromagnetic simulations, they do not remain static but exhibit a slow spatial drift or gradual deformation. A state

is considered to be in a true numerical equilibrium only when the torque acting on the magnetization vanishes, satisfying the condition:

$$\mathbf{m} \times \mathbf{H}^{\text{eff}} = 0. \quad (6)$$

Here, the effective field \mathbf{H}_{eff} is defined as the functional derivative of the total energy E_{total} with respect to the magnetization¹⁶:

$$\mathbf{H}^{\text{eff}} = -\frac{1}{\mu_0 M_s} \frac{\delta E_{\text{total}}}{\delta \mathbf{m}}. \quad (7)$$

While the reconstructed structures do not abruptly collapse, which indicates that they reside in a low-energy region of the state space, a perfect numerical equilibrium was difficult to reach. This once again points toward discrepancies between the experimental sample (e.g., local pinning sites) and the simulation model, which prevent the discovery of a strictly static solution.

Finally, in the present work the material parameters were taken from literature¹⁷ and kept fixed during the reconstruction. Quantitative errors in these parameters can propagate to the optimization results: for example, a misestimate of saturation magnetization (M_s) or sample thickness will likely result in an incorrect reconstruction of the sensor height d_{NV}^* . Similarly, the reconstruction results depend heavily on the choice of micromagnetic interactions included in the model. For instance, the inclusion and sign of the interfacial Dzyaloshinskii-Moriya interaction (DMI) directly dictates the chirality and type of domain walls observed in the solution. Consequently, omitting relevant energy terms (such as the DMI) can lead to qualitatively incorrect textures. Ultimately, this dependence on prior knowledge represents a double-edged sword. On the one hand, incorrect physical inputs yield flawed reconstructions. On the other hand, this sensitivity offers a pathway for identifying the correct physics. Nevertheless, this inverse approach faces an inherent limitation: if multiple sets of physical assumptions result in stray fields that explain the measurement data equally well, then our measurement alone lacks the necessary information content to uniquely determine the underlying magnetic state.

V. CONCLUSION

Our physics-informed framework infers complex magnetic textures, such as skyrmions, from NV magnetometry data by utilizing total micromagnetic energy as a regularization constraint within a continuous height-dependent forward model. This enables the joint optimization of the sensor-sample distance, a central advantage that eliminates the need for calibration procedures. Furthermore, we strictly enforce a normalized magnetization via Riemannian optimization on the unit sphere manifold. The simple formulation of the method allows us to use the L-Curve method to provide a straightforward procedure for balancing data fidelity with energy considerations. Beyond valid reconstruction, this framework opens new pathways for material characterization. The sensitivity of the reconstruction to the underlying energy terms suggests that this method could be utilized for magnetic source identification. By observing which physical model best stabilizes the solution, we can potentially distinguish the specific energy terms and physical mechanisms. While challenges regarding non-uniqueness remain, this physics-based approach offers a powerful tool for quantitative magnetic imaging.

ACKNOWLEDGMENTS

This research was funded in whole, or in part, by the Austrian Science Fund (FWF) 10.55776/PIN1629824, 10.55776/P34671, and 10.55776/PAT3864023 (IMECS). The computational results presented were achieved using the Vienna Scientific Cluster (VSC-5). For the purpose of open access, the author has applied a CC BY public copyright license to any Author Accepted Manuscript version arising from this submission.

AUTHOR CONTRIBUTIONS

A.S. conceptualized the specific physics-informed reconstruction framework, implemented the method, performed the synthetic and experimental evaluations, and wrote the original manuscript. This work builds upon the foundational concept of inverse micromagnetics established by F.B. and C.A., who developed the core inverse micromagnetic simulation software `magnum.np`. C.A., D.S. and F.B. also directly contributed to the development of the methodology. On the experimental side, data acquisition was performed by Y.-G.C., H.B., L.B., C.D., and U.V. The NV magnetometry infrastructure is overseen by C.D. and U.V. Additionally, Y.-G.C., U.V. and C.A. supported the application of the method to the experimental data, including the configuration of simulation parameters and the interpretation of the results. All authors engaged in scientific discussions and reviewed the manuscript.

REFERENCES

- ¹F. Casola, T. van der Sar, and A. Yacoby, “Probing condensed matter physics with magnetometry based on nitrogen-vacancy centres in diamond,” *Nature Reviews Materials* **3**, 17088 (2018).
- ²Y. Xu, W. Zhang, and C. Tian, “Recent advances on applications of NV⁻ magnetometry in condensed matter physics,” *Photonics Research* **11**, 393–412 (2023).
- ³G. E. Backus, “Non-uniqueness of the external geomagnetic field determined by surface intensity measurements,” *Journal of Geophysical Research (1896-1977)* **75**, 6339–6341 (1970), eprint: <https://agupubs.onlinelibrary.wiley.com/doi/pdf/10.1029/JA075i031p06339>.
- ⁴F. Bruckner, C. Abert, G. Wautischer, C. Huber, C. Vogler, M. Hinze, and D. Suess, “Solving Large-Scale Inverse Magnetostatic Problems using the Adjoint Method,” *Scientific Reports* **7**, 40816 (2017).
- ⁵C. B. Clement, J. P. Sethna, and K. C. Nowack, “Reconstruction of Current Densities from Magnetic Images by Bayesian Inference,” (2021), arXiv:1910.12929 [physics].
- ⁶H. J. Hug, B. Stiefel, P. J. A. van Schendel, A. Moser, R. Hofer, S. Martin, H.-J. Güntherodt, S. Porthun, L. Abelmann, J. C. Lodder, G. Bochi, and R. C. O’Handley, “Quantitative magnetic force microscopy on perpendicularly magnetized samples,” *Journal of Applied Physics* **83**, 5609–5620 (1998).
- ⁷Y. Feng, A.-O. Mandru, O. Yildirim, and H. Hug, “Quantitative Magnetic Force Microscopy: Transfer-Function Method Revisited,” *Physical Review Applied* **18**, 024016 (2022).
- ⁸C. Yao, Y. Yu, Y. Shi, J.-I. Jung, Z. Váci, Y. Wang, Z. Liu, C. Zhang, S. Tikoo-Schantz, and C. Zu, “Universal reconstruction of complex magnetic profiles with minimal prior assumptions,” *Physical Review Applied* **24**, 064020 (2025).
- ⁹D. A. Broadway, M. Flaks, A. E. Dubois, and P. Maletinsky, “Reconstruction of nontrivial magnetization textures from magnetic field images using neural networks,” *Physical Review Applied* **23**, 044012 (2025).
- ¹⁰A. Dubois, D. Broadway, A. Stark, M. Tschudin, A. Healey, S. Huber, J.-P. Tetienne, E. Greplova, and P. Maletinsky, “Untrained Physically Informed Neural Network for Image Reconstruction of Magnetic Field Sources,” *Physical Review Applied* **18**, 064076 (2022).
- ¹¹D. Suess, A. Setescaj, J. Smith, F. Bruckner, H. J. Hug, and C. Abert, “Reconstruction of magnetic structures and material parameters with convolutional neural network and bias field-constrained micro-magnetic relaxation,” *Scientific Reports* **15**, 42867 (2025).
- ¹²P. C. Hansen and D. P. O’Leary, “The Use of the L-Curve in the Regularization of Discrete Ill-Posed Problems,” *SIAM Journal on Scientific Computing* **14**, 1487–1503 (1993).
- ¹³D. Calvetti, S. Morigi, L. Reichel, and F. Sgallari, “Tikhonov regularization and the L-curve for large discrete ill-posed problems,” *Journal of Computational and Applied Mathematics Numerical Analysis 2000. Vol. III: Linear Algebra*, **123**, 423–446 (2000).
- ¹⁴F. Bruckner, S. Koraltan, C. Abert, and D. Suess, “magnum.np: a PyTorch based GPU enhanced finite difference micromagnetic simulation framework for high level development and inverse design,” *Scientific Reports* **13**, 12054 (2023).
- ¹⁵L. Rondin, J.-P. Tetienne, T. Hingant, J.-F. Roch, P. Maletinsky, and V. Jacques, “Magnetometry with nitrogen-vacancy defects in diamond,” *Reports on Progress in Physics* **77**, 056503 (2014).
- ¹⁶C. Abert, “Micromagnetics and spintronics: models and numerical methods,” *The European Physical Journal B* **92**, 120 (2019).
- ¹⁷C. Zhang, Z. Jiang, J. Jiang, W. He, J. Zhang, F. Hu, S. Zhao, D. Yang, Y. Liu, Y. Peng, H. Yang, and H. Yang, “Above-room-temperature chiral skyrmion lattice and Dzyaloshinskii–Moriya interaction in a van der Waals ferromagnet $Fe_{3-x}GaTe_2$,” *Nature Communications* **15**, 4472 (2024).
- ¹⁸A. Paszke, S. Gross, F. Massa, A. Lerer, J. Bradbury, G. Chanan, T. Killeen, Z. Lin, N. Gimelshein, L. Antiga, A. Desmaison, A. Köpf, E. Yang, Z. DeVito, M. Raison, A. Tejani, S. Chilamkurthy, B. Steiner, L. Fang, and S. Chintala, *PyTorch: An Imperative Style, High-Performance Deep Learning Library* (2019).

- ¹⁹M. Kochurov, R. Karimov, and S. Kozlukov, “GeoOpt: Riemannian Optimization in PyTorch,” (2020), arXiv:2005.02819 [cs].
- ²⁰D. P. Kingma and J. Ba, “Adam: A Method for Stochastic Optimization,” (2017), arXiv:1412.6980 [cs].
- ²¹magnum.np developers, “Inverse Problems — magnum.np 2.2.0 documentation,” https://magnum.np.gitlab.io/magnum.np/inverse_problems.html (2026), accessed: 2026-02-18.
- ²²Z. Xu, M. L. Palm, W. Huxter, K. Herb, J. M. Abendroth, K. Bouzheouane, O. Boule, M. S. Gabor, J. Urrestarazu Larranaga, A. Morales, J. Rhensius, G. Puebla-Hellmann, and C. L. Degen, “Minimizing Sensor-Sample Distances in Scanning Nitrogen-Vacancy Magnetometry,” *ACS Nano* **19**, 8255–8265 (2025).
- ²³L. D. Landau and E. M. Lifshitz, “Theory of the dispersion of magnetic permeability in ferromagnetic bodies,” *Physikalische Zeitschrift der Sowjetunion* **8**, 153–169 (1935).
- ²⁴T. L. Gilbert, “A phenomenological theory of damping in ferromagnetic materials,” *IEEE Transactions on Magnetics* **40**, 3443–3449 (2004).
- ²⁵R. Bodenberger and A. Hubert, “Zur bestimmung der blochwandenergie von einachsigen ferromagneten,” *physica status solidi (a)* **44**, K7–K11 (1977), eprint: <https://onlinelibrary.wiley.com/doi/pdf/10.1002/pssa.2210440146>.
- ²⁶A. Hubert and R. Schäfer, *Magnetic domains: the analysis of magnetic microstructures*, softcover reprint of the hardcover 1st ed. 1998, corrected printing 2000 ed. (Springer, Berlin Heidelberg, 2014).
- ²⁷S. Rohart and A. Thiaville, “Skyrmion confinement in ultrathin film nanostructures in the presence of Dzyaloshinskii-Moriya interaction,” *Physical Review B* **88**, 184422 (2013).

Appendix A: Analysis of ODMR Sign Ambiguity Artefacts

We analyse the NV magnetometry datasets of the $\text{Fe}_{3-x}\text{GaTe}_2$ sample to evaluate the impact of Optically Detected Magnetic Resonance (ODMR) sign ambiguity artefacts. NV magnetometry probes the projection of the local magnetic field onto the quantization axis of the nitrogen–vacancy (NV) center. Each NV center defines a fixed crystallographic axis \mathbf{n}_{NV} along one of the four $\langle 111 \rangle$ directions of the diamond lattice. In the present measurements, a single NV orientation is addressed, whose axis lies in the x – z plane at an angle of $\theta = 55^\circ$ relative to the sample normal (z -axis):

$$\mathbf{n}_{\text{NV}} = (\sin \theta, 0, \cos \theta). \quad (\text{A1})$$

The magnetic field component sensed by the NV is therefore the scalar projection of the total magnetic field onto this axis,

$$H_{\parallel} = (\mathbf{H}^{\text{bias}} + \mathbf{H}^{\text{dem}}) \cdot \mathbf{n}_{\text{NV}}, \quad (\text{A2})$$

where \mathbf{H}^{bias} denotes the applied external bias field and \mathbf{H}^{dem} the sample stray field.

ODMR spectroscopy does not directly measure H_{\parallel} , but rather the Zeeman splitting of the NV electronic spin resonances. In the presence of a magnetic field component along \mathbf{n}_{NV} , the $m_s = \pm 1$ spin states split symmetrically around the zero-field splitting, resulting in a frequency separation

$$\Delta f = 2\gamma_{\text{NV}}|H_{\parallel}|, \quad (\text{A3})$$

where γ_{NV} is the NV gyromagnetic ratio¹⁵. Since ODMR is sensitive only to the magnitude of the frequency splitting, it yields $|H_{\parallel}|$ and is intrinsically insensitive to the sign of the projected magnetic field along the NV axis. A bias field is therefore required for quantitative imaging, as it defines a reference direction and lifts the degeneracy of the spin transitions. In our analysis, we define the reported measurement field H^{meas} , displayed in Fig. A1, as the total field magnitude minus the bias contribution:

$$H^{\text{meas}} = |H_{\parallel}| - H^{\text{bias}}. \quad (\text{A4})$$

Under ideal conditions, where $H_{\parallel} > 0$ across the entire scan, this simplifies to $H^{\text{meas}} = H^{\text{dem}}$. However, if the sample stray field locally opposes and exceeds the applied bias field ($H^{\text{dem}} < -H^{\text{bias}}$), the term $|H_{\parallel}|$ undergoes a sign inversion.

As presented in Fig. A1, the pixel value histograms (in kA/m) therefore reveal a pronounced asymmetry between positive and negative field values. In Measurement 2, positive values extend to approximately 10 kA/m, whereas negative values exhibit an abrupt cutoff near -4 kA/m. This cutoff corresponds approximately to the magnitude of the applied bias field. In practice, \mathbf{H}^{bias} is not perfectly spatially homogeneous, and small variations in its magnitude across the field of view imply that the precise threshold for sign inversion varies locally. Consequently, instead of marking a single threshold value, we highlight the lowest 10% of field values in green. This interval represents a critical regime where the total projected field approaches zero, $|H^{\text{bias}} + H^{\text{dem}}| \approx 0$, and ODMR sign ambiguity artefacts are most likely to occur.

The impact of this ambiguity is clearly visible in the one-dimensional line cuts. Under artifact-free conditions, the stray field exhibits smooth, approximately parabolic local minima. In Measurement 2, however, several profiles display deep minima that are rectified into characteristic W-shaped features, as observed in Lines A, D, E, and F. These profiles indicate regions where H^{dem} locally opposed and exceeded H^{bias} , causing the measured signal to fold back as the true field crossed zero. In contrast, Measurement 1 was acquired at a larger sensor–sample distance, resulting in smaller stray-field amplitudes. As illustrated by Line B, the corresponding field profiles form plateaus rather than sharp inversions, indicating that the total projected field approaches but does not significantly cross the sign-reversal threshold.

This comparison also enables the validation of subtler magnetic features. For example, the smaller magnetic field texture intersected by Line C is confirmed to be a genuine feature rather than an artefact, as its local minimum remains well separated from the artifact-prone signal range. Given the minimal presence of critical ODMR sign ambiguity artefacts, Measurement 1 was selected for the magnetization reconstruction.

Appendix B: Detailed Simulation Setup

The micromagnetic simulations were conducted using a finite-difference discretization. To ensure the numerical model accurately reproduces the experimental behavior of the $\text{Fe}_{3-x}\text{GaTe}_2$ flake, we selected material parameters based on recent literature and the mesh discretization based on characteristic length scales.

1. Material Parameters

The material parameters at $T = 295\text{ K}$ are adopted from recent work characterizing the same $\text{Fe}_{3-x}\text{GaTe}_2$ flake¹⁷. They report an exchange stiffness of $A \approx 0.70\text{ pJ m}^{-1}$, an effective anisotropy of $K_{\text{eff}} \approx 0.30\text{ MJ m}^{-3}$ and an interfacial Dzyaloshinskii-Moriya interaction constant of $D_i \approx -0.51\text{ mJ m}^{-2}$. The saturation magnetization, M_s , is derived via a phenomenological domain wall model²⁵. By matching the experimentally observed domain wall width w and energy density δ_w , M_s is calculated as:

$$M_s = \sqrt{\frac{4\pi\beta\delta_w}{\mu_0 w}} \approx 53\text{ kA m}^{-1}, \quad (\text{B1})$$

where $\delta_w = 0.22\text{ mJ m}^{-2}$, $w = 0.24\text{ }\mu\text{m}$ ¹⁷, μ_0 is the vacuum permeability and β is a phenomenological fitting parameter that is approximately 0.31 for magnets with high magnetocrystalline anisotropy¹⁷. The effective anisotropy K_{eff} aggregates both crystalline and shape contributions. However, micromagnetic solvers already calculate the demagnetizing field (shape anisotropy). To avoid double-counting this energy, we need to calculate the intrinsic crystalline anisotropy K_{u} , which is then to be used as the simulation input:

$$K_{\text{u}} = K_{\text{eff}} + \frac{1}{2}\mu_0 M_s^2. \quad (\text{B2})$$

This relation isolates K_{u} by re-adding the shape anisotropy energy component subtracted in the effective anisotropy formulation²⁶. This relation is only valid for thin films with out-of-plane uniaxial anisotropy, where the demagnetizing factors are approximately $N_z = 1$ and $N_x = N_y = 0$.

2. Discretization and Geometry

The spatial discretization was determined by the characteristic magnetic length scales of the system, specifically the exchange length²⁶, $l_{\text{ex}} = \sqrt{A/K_{\text{eff}}}$, and the DMI length²⁷, $l_{\text{D}} = 2A/|D|$. To resolve the magnetic texture accurately, the lateral cell size was set to $\Delta_x = \Delta_y = 1\text{ nm}$.

The full simulation domain is defined by a grid of $N_x \times N_y \times N_z = 900 \times 900 \times 2$ cells. Along the surface normal, the discretization is $\Delta_z = 100\text{ nm}$. The geometry consists of two layers: the bottom layer represents the magnetic material, while the top layer is set to vacuum for computation of stray fields above the sample surface. To mitigate boundary artifacts, the simulation grid (900×900) includes a 50 cell (50 nm) padding on all lateral sides relative to the region of interest (800×800).

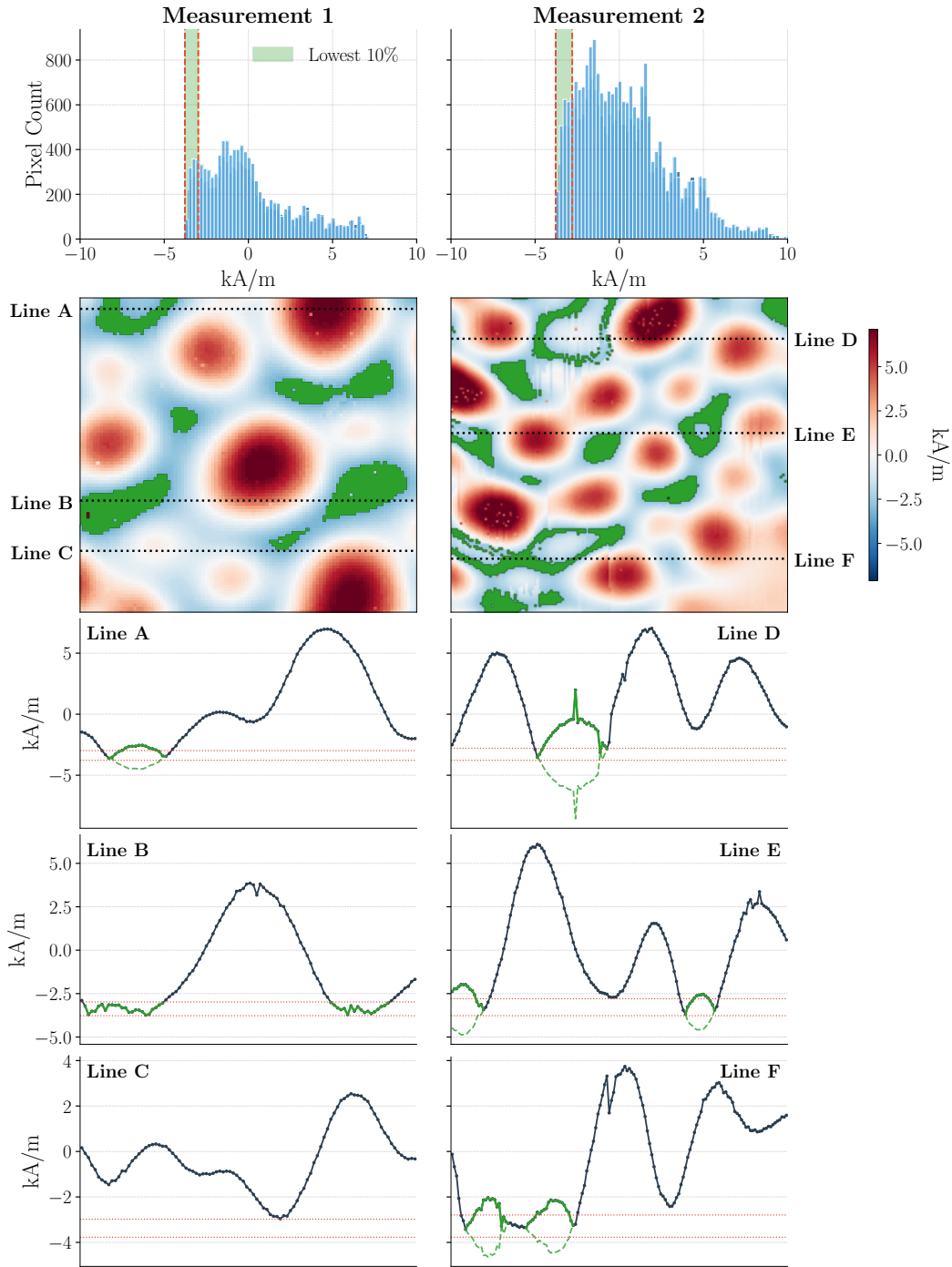


FIG. A1: **Analysis of ODMR sign ambiguity artifacts.** Histograms show the magnetic field pixel value distributions for Measurement 1 and Measurement 2. The red dashed lines mark the 0th and 10th percentiles of the field distribution; the green shaded region in the histogram and in the field maps represent the lowest 10% of pixel values. The same percentile thresholds are indicated in the corresponding 1D line cuts (A–F) with red dashed lines. These line cuts illustrate field profiles across selected features, distinguishing artifact-free behavior (Line C), plateau formation (Line B), and folded artifacts (Lines A, D, E, F). In the 1D line plots, solid green segments indicate the artifacts in the measurement and the green dashed lines represent how the magnetic field likely looked in reality.

3. Post-Processing

To enable a direct pixel-to-pixel comparison between the simulation and experimental measurements, the high-resolution simulation data was post-processed to match the experimental spatial resolution. The experimental field of view (FOV) for Measurement 1 consists of 100×100 pixels with a physical pixel size of 8 nm. Since the raw simulation output used a finer resolution of 1 nm per pixel, the data was downsampled. This was achieved by averaging 8×8 blocks of simulation pixels into a single representative pixel value, ensuring both datasets share the same sampling grid for further analysis.

Appendix C: Derivation of the Fourier-Space Upward Continuation Operator

This section details the analytical derivation of the transfer function used to upward continue magnetic stray fields from a discretized simulation grid to an arbitrary measurement height. This formulation accounts for the finite volume averaging inherent in finite-difference discretizations and allows for continuous differentiability with respect to the sensor position.

1. Magnetostatic Governing Equations in Fourier Space

In a source-free region above a magnetic sample, the magnetic field \mathbf{H} satisfies Maxwell's equations for magnetostatics:

$$\nabla \times \mathbf{H} = 0, \quad (\text{C1})$$

$$\nabla \cdot \mathbf{H} = 0. \quad (\text{C2})$$

The curl-free condition implies that the field can be expressed as the gradient of a magnetic scalar potential, $\mathbf{H} = -\nabla\Phi$. Substituting this into the divergence-free condition yields Laplace's equation:

$$\nabla^2\Phi = 0. \quad (\text{C3})$$

We define the geometry such that the magnetic material is confined to the half-space $z < z_0$, and the region $z > z_0$ is free space. To solve this, we apply a two-dimensional Fourier transform over the lateral coordinates (x, y) :

$$\tilde{\Phi}(k_x, k_y, z) = \frac{1}{2\pi} \int_{-\infty}^{\infty} \int_{-\infty}^{\infty} \Phi(x, y, z) e^{-i(k_x x + k_y y)} dx dy. \quad (\text{C4})$$

In Fourier space, Laplace's equation becomes an ordinary differential equation in z :

$$\left(\frac{\partial^2}{\partial z^2} - k^2 \right) \tilde{\Phi}(k, z) = 0, \quad (\text{C5})$$

where $k = \sqrt{k_x^2 + k_y^2}$ is the magnitude of the in-plane wave vector. For the region $z > z_0$, we require the potential to vanish as $z \rightarrow \infty$. Consequently, the physical solution is restricted to the decaying exponential branch:

$$\tilde{\Phi}(k, z) = \tilde{\Phi}(k, z_0) e^{-k(z-z_0)}. \quad (\text{C6})$$

Since the magnetic field components are spatial derivatives of the potential ($\tilde{H}_x = -ik_x \tilde{\Phi}$, $\tilde{H}_y = -ik_y \tilde{\Phi}$, $\tilde{H}_z = k \tilde{\Phi}$), every component of the magnetic field vector $\tilde{\mathbf{H}}$ follows the exact same exponential decay law as the potential:

$$\tilde{\mathbf{H}}(z) = \tilde{\mathbf{H}}(z_0) e^{-k(z-z_0)}. \quad (\text{C7})$$

2. Correction for Cell-Averaging

In finite-difference micromagnetic simulations, the computed stray field \mathbf{H}^{dem} is typically not a point value at a specific height z , but rather a volume-averaged value over a discretization cell of vertical thickness Δ_z .

We define the averaged field $\langle \tilde{\mathbf{H}} \rangle$ over a vacuum layer of thickness Δ_z , extending from the sample surface z_0 to $z_0 + \Delta_z$, as follows¹⁶:

$$\langle \tilde{\mathbf{H}} \rangle_{[z_0, z_0 + \Delta_z]} = \frac{1}{\Delta_z} \int_{z_0}^{z_0 + \Delta_z} \tilde{\mathbf{H}}(z) dz \quad (\text{C8})$$

Substituting the analytical decay behavior from Eq. (C7) into this integral yields:

$$\langle \tilde{\mathbf{H}} \rangle_{[z_0, z_0 + \Delta_z]} = \frac{\tilde{\mathbf{H}}(z_0)}{\Delta_z} \int_{z_0}^{z_0 + \Delta_z} e^{-k(z-z_0)} dz \quad (\text{C9})$$

$$= \frac{\tilde{\mathbf{H}}(z_0)}{\Delta_z} \left[-\frac{1}{k} e^{-k(z-z_0)} \right]_{z_0}^{z_0 + \Delta_z} \quad (\text{C10})$$

$$= \tilde{\mathbf{H}}(z_0) \left(\frac{1 - e^{-k\Delta_z}}{k\Delta_z} \right). \quad (\text{C11})$$

This expression relates the discrete simulation output $\langle \tilde{\mathbf{H}} \rangle$ to the exact field value at the surface $\tilde{\mathbf{H}}(z_0)$. By inverting this relationship, we obtain a de-averaging factor that reconstructs the surface field:

$$\tilde{\mathbf{H}}(z_0) = \langle \tilde{\mathbf{H}} \rangle_{[z_0, z_0 + \Delta_z]} \cdot \left(\frac{k\Delta_z}{1 - e^{-k\Delta_z}} \right). \quad (\text{C12})$$

3. Upward Continuation

To determine the magnetic field at an arbitrary height z (where $z > z_0$), we apply the standard upward continuation operator to the reconstructed surface field $\tilde{\mathbf{H}}(z_0)$:

$$\tilde{\mathbf{H}}(z) = \tilde{\mathbf{H}}(z_0) \cdot e^{-k(z-z_0)}. \quad (\text{C13})$$

Substituting Eq. (C12) into Eq. (C13) provides the complete transfer function:

$$\tilde{\mathbf{H}}(z) = \langle \tilde{\mathbf{H}} \rangle_{[z_0, z_0 + \Delta_z]} \cdot \left(\frac{k\Delta_z}{1 - e^{-k\Delta_z}} \right) \cdot e^{-k(z-z_0)}, \quad (\text{C14})$$

which corresponds to the final model presented in Eq. (1). The final magnetic field distribution in real space, $\mathbf{H}(z)$, is recovered via the inverse 2D Fourier transform. This formulation ensures that the simulated signal is explicitly differentiable with respect to the measurement height z , enabling gradient-based optimization of the sensor position.